

Supplementary Information

Structure of a Force-Conveying Cadherin Bond Essential for Inner-Ear Mechanotransduction

Marcos Sotomayor, Wilhelm A. Weihofen, Rachelle Gaudet, David P. Corey

Supplementary Discussion

Cadherin dissociation constants

Reported K_D values for classical cadherins⁵⁰⁻⁵² have been measured using analytical ultracentrifugation and range from ~ 1 to ~ 100 μM at 25°C . Measurements for type II cadherins indicate K_D values in the lower μM range, while values for type I cadherins are usually >20 μM . For instance, a type II VE-cadherin construct with 5 EC repeats has a K_D of 1 μM at 25°C ⁵², while K_D values for type I N-cadherin EC1+2 are ~ 26 μM at 25°C ⁵¹. Interestingly, some classical cadherin K_D values are temperature dependent (values for type I E-cadherin EC1+2 at 25°C and 37°C differ almost two-fold: 96.5 ± 10.6 to 160 ± 21.3 μM), while others (N-cadherin) are temperature independent⁵¹. Our ITC measurements at 10°C indicate that the pcdh-15+cdh-23 bond is entropy-driven, suggesting temperature-dependence such that its K_D could be < 1 μM at 37°C . The K_D of 2.9 μM reported here for pcdh-15+cdh-23 is in the lower range of the values measured for classical type II cadherins, although a proper comparison would require matching techniques and experimental conditions.

Predictions from simulations, tip link mechanics, and physiological time scales

Molecular dynamics simulations have usually been limited to nanoseconds, with SMD simulations using non-physiological stretching speeds to induce conformational changes within this achievable time scale⁴². However, even when using such fast pulling speeds, SMD simulations have correctly predicted the mechanical properties of multiple proteins, such as ankyrin⁵³ and C-cadherin⁴³, as determined by subsequent (independent) AFM experimental work pulling directly on them⁵⁴⁻⁵⁶. Transduction in the auditory system can be extremely fast⁵⁷ (< 10 μs), presenting an interesting challenge for both SMD simulations and AFM experiments. *In vivo* laser-velocimetry measurements of basilar membrane mechanics (10 to 100 dB at or near the 10 kHz characteristic frequency)²³ show motion at speeds of 10^{-5} to 10^{-2} nm/ns. In addition, experimental stimulation of hair-cell bundles is usually performed at speeds that can reach up to 0.018 nm/ns²⁴. We therefore reduced the simulated stretching speed to 0.02 nm/ns, extending the time scale of our simulations to hundreds of nanoseconds (15 ns/day of computing). Thus, the SMD simulations reported here explore the response of tip-link proteins to stimuli like those of loud sound, while still providing insights into the force-bearing elements of the bond formed by pcdh-15 and cdh-23. Alternative pulling experiments can only complement our results, as the AFM cantilever can only reach pulling speeds $< 10^{-5}$ nm/ns, covering low frequency or weak sound-like stimuli. In addition, these types of experiments only provide limited information about the structural and molecular details of forced unbinding and unfolding pathways. While our simulation results are still limited by force-field imperfections and model assumptions⁵⁸, we expect that they will guide the interpretation of the experimental exploration of the tip link's mechanical properties and the pcdh-15+cdh-23 bond.

Dynamics of pcdh-15 and cdh-23 contacts during unbinding

Trajectories of pcdh-15+cdh-23 forced unbinding were monitored to determine which molecular events were correlated with detachment and associated force peaks. In all our

simulations with bound Ca^{2+} , full detachment of one protomer from the other was preceded by rupture of contacts other than those mediated by residues near R113 in pcdh-15 (see green arrows in Fig. 3a and Supplementary Fig. 10a), by sliding of residues located near a 3_{10} helix within strand A of cadherin-23 EC1 (Y16, L18) over the RXGPP loop of pcdh-15 (Fig. 3a,b and Supplementary Fig. 10a-c), and finally by rupture of the pcdh-15_{R113} – cdh-23_{E77} salt bridge. In some cases further transient and weak interactions between the N-termini of pcdh-15 and cdh-23 ensued. We further analyzed the two slowest SMD simulations, SN6 and SNA7, which started from different initial conditions, by monitoring distances between residues at four locations: the tip of pcdh-15 and the adjacent EC2 repeat of cdh-23 (pcdh-15_{T106} – cdh-23_{L145}); the center of the interface (pcdh-15_{R113} – cdh-23_{E77} and pcdh-15_{I22} – cdh-23_{Y16}); and the tip of cdh-23 and the adjacent residues in pcdh-15 (pcdh-15_{R84} – cdh-23_{N96}). Distances plotted in Supplementary Fig. 11 confirmed the sequence of events described above. While the pcdh-15_{R113} – cdh-23_{E77} salt bridge seems to break last, it is unclear whether its head-to-head conformation facilitates sliding or actually provides resistance during unbinding. Interestingly, unbinding forces for all simulations in which the complex was equilibrated over 1 μs were slightly larger than those monitored for simulations in which the same complex was equilibrated for only 1 ns. This was correlated with an increase in interface area during equilibration (Supplementary Fig. 14).

Unbinding and unfolding of tip-link EC repeats

In simulations performed with Ca^{2+} -bound proteins, unbinding forces between pcdh-15 and cdh-23 are smaller than forces required to unfold EC1+EC2 repeats¹⁶. Therefore, under normal conditions, our simulations predict that the two tip-link cadherins unbind before either unfolds. However, pcdh-15+cdh-23 unbinding forces are similar to unfolding forces in the absence of Ca^{2+} . Thus unfolding may occur before unbinding when EC repeats cannot bind Ca^{2+} . Indeed, stretching simulations of the Ca^{2+} -free complex showed unfolding of EC repeats before unbinding at almost all stretching speeds (Supplementary Fig. 17). At the slowest stretching speed (0.1 nm/ns), the complex separated before EC repeats unfolded, yet linker regions in both protomers were completely extended and exposed with partial unfolding of some β -strands before complex separation. Deafness mutations impairing Ca^{2+} binding in EC repeats not directly involved in the interface between protocadherin-15 and cadherin-23 may weaken the tip-link without affecting complex formation, by promoting unfolding before unbinding upon mechanical stimulation^{43,59}. The exposure of the naked linkers and unfolding of repeats might also have deleterious effects in the long term, with misfolding or enzyme-mediated degradation causing malfunction of tip-links with impaired Ca^{2+} -binding capabilities.

Molecular mechanisms of Ca^{2+} dependence

To reveal the molecular mechanisms underlying dissociation upon Ca^{2+} removal we performed microsecond-long molecular dynamics simulations⁴⁴ of the pcdh-15+cdh-23 structure S1b. Simulations with bound Ca^{2+} , lasting over 1 μs , showed a stable system with RMSD values < 4.4 Å for the complex, < 3 Å for cdh-23, and < 3.8 Å for pcdh-15 (Supplementary Fig. 13). In contrast, the simulated complex without bound Ca^{2+} was not stable and RMSD quickly reached values >> 5 Å. The complex did not dissociate during

the simulations, but rather became deformed due to inter-repeat motion of individual protomers (Supplementary Figs 13b,c & 14, and Movies III&IV). Individual EC repeats did retain their fold, with RMSD values not exceeding 3.6 Å (Supplementary Fig. 13d). In one of the simulations performed in the absence of Ca^{2+} we observed loss of some of the native contacts seen in the crystal structure (Supplementary Movie V). Thus, the complex may unbind in the absence of Ca^{2+} at longer time scales as a consequence of the increased dynamics of individual components (entropic stress). Unbinding may also be accelerated by other factors such as tension in the tip link. Overall, the simulations predict the existence of a transient Ca^{2+} -free complex and show how Ca^{2+} provides rigidity for each EC1-EC2 linker, which in turn maintains the binding interface of pcdh-15+cdh-23. Loss of Ca^{2+} from sites 1, 2 and 3 makes the EC-EC junction less rigid, and flexion then distorts the binding interface. This mechanism may apply to classical cadherins as well^{25,60-62}, where transient Ca^{2+} -free dimers have been recently reported^{63,64}.

Molecular mechanisms underlying inherited deafness

Four deafness mutations are located within the crystallized pcdh-15+cdh-23 complex: pcdh-15_{D157G}, cdh-23_{D101G}, pcdh-15_{R113G}, and cdh-23_{S47P}. Pcdh-15 residue D157 coordinates Ca^{2+} at site 3 and D157G may severely impair folding and/or Ca^{2+} binding, as has been shown for an equivalent D134A mutation in N-cadherin⁶⁵. Consistently, the pcdh-15_{D157G} fragment did not co-refold with wild-type cdh-23 (Supplementary Fig. 2c). The cdh-23 D101 sidechain coordinates Ca^{2+} at site 2 and we showed experimentally¹⁶ that D101G decreases affinity for Ca^{2+} . Although D101 is at the interface between pcdh-15 and cdh-23, the sidechain does not participate in interactions with pcdh-15. Consistently, the cdh-23_{D101G} mutant co-refolded and interacted with pcdh-15 just like wild-type cdh-23 in SEC at 1 mM CaCl_2 (Supplementary Fig. 2c,d). Yet ITC experiments show decreased affinity between pcdh-15 and cdh-23_{D101G} (Fig. 2c). A crystal structure of pcdh-15+cdh-23_{D101G} does not show significant changes at the interface (overall backbone RMSD 0.32 Å, Supplementary Fig. 16a). Thus, increased flexibility at the linker of cdh-23, even in the presence of bound Ca^{2+} , may explain altered binding¹⁶. At very low Ca^{2+} concentrations, this mutation may further impair complex formation or accelerate unfolding of a tip-link EC repeat during mechanical stimulation, as seen in our SMD simulations of the complex without bound Ca^{2+} (Supplementary Discussion above and Supplementary Fig. 17). In contrast to the previous mutations and to R113G (discussed in the main text), S47P in cdh-23 did not affect complex formation with pcdh-15 in either SEC or ITC experiments ($N = 0.86$; $K_D = 2.4 \mu\text{M}$, $T = 10^\circ\text{C}$, $\Delta H = 7181 \text{ cal/mol}$, $\Delta S = 51.1 \text{ cal/mol/deg}$; Fig. 2c and Supplementary Figs 2c,d, 8 & 16). Moreover, this mutation is not expected to affect Ca^{2+} binding as it is not located near a Ca^{2+} -binding site nor does it modify a charged residue. A crystal structure of pcdh-15+cdh-23_{S47P} does not show significant changes at the interface (overall backbone RMSD 0.2 Å). However, a β -strand forming hydrogen bond is disrupted by this mutation, with a water molecule supplying the missing interaction and pushing the backbone of S47P away from the protomer (Supplementary Fig. 16). Thus, S47P may have a more subtle effect on the structural stability of the cdh-23 EC1 repeat, or may instead disrupt protein synthesis, processing, or localization.

Interestingly, the different biochemical effects of deafness mutations studied here correlate with the severity of the inner-ear phenotype. We were unable to co-refold the

pcdh-15_{D157G} fragment, which causes both profound deafness and vestibular dysfunction. Mutations pcdh-15_{R113G} and cdh-23_{D101G} impaired but did not abolish complex formation and Ca²⁺ binding, respectively, and both cause severe to profound deafness but without obvious phenotype in the less mechanically-demanding vestibular system^{27,28}. Lastly, the cdh-23_{S47P} mutation did not produce any obvious biochemical effects, but rather a subtle structural effect that is consistent with its possible role in progressive rather than severe hearing loss²⁹. Our data also suggest treatments in certain cases. Increase in Ca²⁺ concentration of the endolymph, or reduced exposure to loud noise might help subjects with mutations D101G and R113G, respectively, but may not be effective for those with the D157G mutation.

Structural determinants of heterophilic contacts

Details of the interaction between pcdh-15 and cdh-23 revealed by our structure, such as the involvement of EC2 repeats, suggest that the current EC1-based phylogenetic classification of the cadherin superfamily may need adjustments, especially if used to determine which members may interact with each other. Here we highlight structural elements and sequence motifs that may define analogous heterophilic cadherin complexes. A long and stable N-terminus, along with an exposed patch of hydrophobic and charged residues, seems to be necessary for a pcdh-15+cdh-23-like heterophilic interface. In addition, key interactions and salt-bridges (such as those between R113 in pcdh-15 and E77/Q98 in cdh-23) may provide the selectivity that prevents the same antiparallel binding for homophilic complexes or favors further overlapping with specific EC repeats (Supplementary Figs 18&19). A simple protein BLAST search for sequence motifs forming the N-termini of pcdh-15 and cdh-23, as well as their heterophilic interface, reveals some candidate heterophilic complexes. While the RXGPP loop at the N-terminus of pcdh-15 is rather unique among cadherins, the pcdh-15 EVRIVVR motif with R113 in the middle (Fig. 2h) is also found in *Mus musculus* fat4 at the same location in EC1 (EVRVLVR). Similarly, a search for the cdh-23 KVNIQV motif with interfacial residues N96 and Q98 (Fig. 2h) reveals an *identical* motif in EC1 of *Mus musculus* fat3. Interestingly, the cdh-23 KSEFT motif with the interfacial residue E77 is also similar to the QDNYL at the same location in EC1 of fat3. These facts, and sequence alignments (data not shown), suggest that fat4 and fat3 share several features important for heterophilic interactions. Analysis of pcdh-21 and pcdh-24 sequences reveals similarities with cdh-23, suggesting that these proteins may form heterophilic complexes with other cadherins. Evidently, a more thorough analysis with homology models is required to determine if pcdh-15+cdh-23-like complexes can be formed by fat3 and fat4, and whether pcdh-21 and pcdh-24 can form heterophilic complexes with other cadherins. However, the sequence motifs and structural elements discussed here provide a first step to search for novel heterophilic cadherin complexes and establish their biological relevance. It would be important to determine if pcdh-15 and cdh-23 can interact with other cadherin molecules as well. Protocadherin-15 is widely expressed in the brain and several tissues including kidney, lung, and pancreas⁶⁶; it may feature polymorphisms positively selected in humans⁶⁷, and has been associated with retinal disorders, lipid abnormalities⁶⁶, and cancer¹⁵. The present study opens the door to exploring its function in different tissues from a structural point of view.

Supplementary Movie Legends

Movie I (A&B)

Forced unbinding of pcdh-15+cdh-23 (simulation SNA7; trajectory shown from $t = 270$ ns up to $t = 336$ ns). Protein is depicted in cartoon representation, with pcdh-15 in purple, cdh-23 in blue, and Ca^{2+} in green. C-terminal C_α atoms are red. Molecular surfaces for pcdh-15 and cdh-23 are shown in transparent purple and blue. Version B shows the same trajectory with opaque molecular surfaces.

Movie II (A&B)

Details of pcdh-15+cdh-23 forced unbinding (simulation SNA7; trajectory shown from $t = 270$ ns up to $t = 336$ ns). Protein is depicted as in Movie I, with residues at the interface shown in stick representation. Molecular surfaces are not shown in movie version A. Version B shows opaque and transparent surfaces for pcdh-15 and cdh-23, respectively.

Movie III

Equilibration of pcdh-15+cdh-23 in the presence of Ca^{2+} (simulation SA1, lasting 1 μs). Protein is depicted in cartoon representation. Pcdh-15 is in purple, cdh-23 in blue, and Ca^{2+} in green.

Movie IV

Equilibration of pcdh-15+cdh-23 in the absence of Ca^{2+} (simulation SA3, lasting 1 μs). Protein is depicted in cartoon representation and colored as in movie III.

Movie V

Dynamics of contacts between pcdh-15 and cdh-23 during equilibrium MD simulations. Contact maps between residue pairs involved in the pcdh-15+cdh-23 interface are shown throughout microsecond-long MD simulations performed in the NpT ensemble with and without Ca^{2+} (SA1 left; SA3 right). The distance between pairs of C_α atoms is displayed using a linear gray scale (0 Å: black; >10 Å: white). A red box highlights location of native contacts lost at the end of simulation SA3 without Ca^{2+} .

Supplementary Tables

Supplementary Table 1. Statistics for pcdh-15+cdh-23 structures

Data Collection and Refinement	Structure S1a	Structure S1b	Structure S2
Space group	C2	C2	C2
Unit cell parameters: a, b, c (Å)	173.61, 40.47, 84.62	173.65, 40.47, 85.19	158.75, 57.03, 156.16
α, β, γ (°)	90, 103, 90	90, 103, 90	90, 99, 90
Molecules per asymmetric unit	1	1	2
Beam source	APS 24-ID-E	ALS 4.2.2	APS 24-ID-E
Wavelength (Å)	0.97949	1.13841	0.97949
Resolution limit (Å)	1.65	2.23	2.63
Unique reflections	66,852 (3,184)	27,442 (1,236)	41,589 (2,017)
Redundancy	3.7 (3.6)	3.4 (2.9)	3.7 (3.6)
Completeness (%)	96.9 (92.8)	96.2 (87.5)	100 (99.8)
Average I/ σ (I)	25.6 (2.8)	10.7 (2.7)	16.9 (2.6)
R _{merge}	0.05 (0.48)	0.10 (0.39)	0.08 (0.51)
Refinement			
Resolution range (Å)	32.03 - 1.65 (1.70 - 1.65)	41.08 - 2.23 (2.29 - 2.23)	38.57 - 2.63 (2.69-2.62)
Residues (atoms)	446 (4,550)	444 (3,924)	889 (7,517)
Water molecules	823	348	480
R _{work} (%)	16.1 (28.7)	17.5 (25.0)	18.9 (34.6)
R _{free} (%)	19.3 (31.7)	23.6 (31.6)	24.3 (38.8)
RMS deviations			
Bond lengths (Å)	0.010	0.017	0.010
Bond angles (°)	1.415	1.543	1.201
B-factor average			
Protein	22.49	29.53	43.18
Ligand/ion	24.52	42.16	31.07
Water	38.41	35.99	41.11
Ramachandran Plot Regions ^a			
Most favored (%)	90.7	90.7	88.5
Additionally allowed (%)	8.8	9.1	10.9
Generously allowed (%)	0.5	0.3	0.6
Disallowed (%)	0.0	0.0	0.0
Interface Area (Å ²)	907	898	1160 1069
PDB ID code	4apx	4axw	4aq8

^aComputed with PROCHECK

Supplementary Table 2. Statistics for mutant pcdh-15+cdh-23 structures

Data Collection and Refinement	Structure S3 pcdh-15+cdh-23 _{D101G}	Structure S4 pcdh-15+cdh-23 _{S47P}
Space group	C2	C2
Unit cell parameters: a, b, c (Å)	173.29, 40.51, 84.63	174.02, 40.87, 84.78
α, β, γ (°)	90, 103, 90	90, 103, 90
Molecules per asymmetric unit	1	1
Beam source	APS 24-ID-E	APS 24-ID-E
Wavelength (Å)	0.97919	0.97919
Resolution limit (Å)	1.96	2.26
Unique reflections	41,729 (1,981)	27,207 (1,318)
Redundancy	3.4 (2.9)	3.5 (3.1)
Completeness (%)	99.4 (95.5)	99.2 (96.8)
Average I/ σ (I)	8.5 (2.4)	9.6 (2.3)
R _{merge}	0.11 (0.40)	0.13 (0.44)
Refinement		
Resolution range (Å)	34.19 – 1.96 (2.00 – 1.96)	22.69 – 2.27 (2.33 – 2.27)
Residues (atoms)	443 (4,155)	444 (3,945)
Water molecules	606	403
R _{work} (%)	17.8 (22.1)	17.3 (20.2)
R _{free} (%)	22.8 (29.9)	23.9 (29.0)
RMS deviations		
Bond lengths (Å)	0.009	0.011
Bond angles (°)	1.327	1.404
B-factor average		
Protein	23.64	24.35
Ligand/ion	20.31	23.29
Water	31.97	28.24
Ramachandran Plot Regions ^a		
Most favored (%)	91.1	90.4
Additionally allowed (%)	8.3	9.4
Generously allowed (%)	0.5	0.3
Disallowed (%)	0.0	0.0
Interface Area (Å ²)	958	895
PDB ID code	4aqa	4aqe

^aComputed with PROCHECK

Supplementary Table 3. Summary of simulations

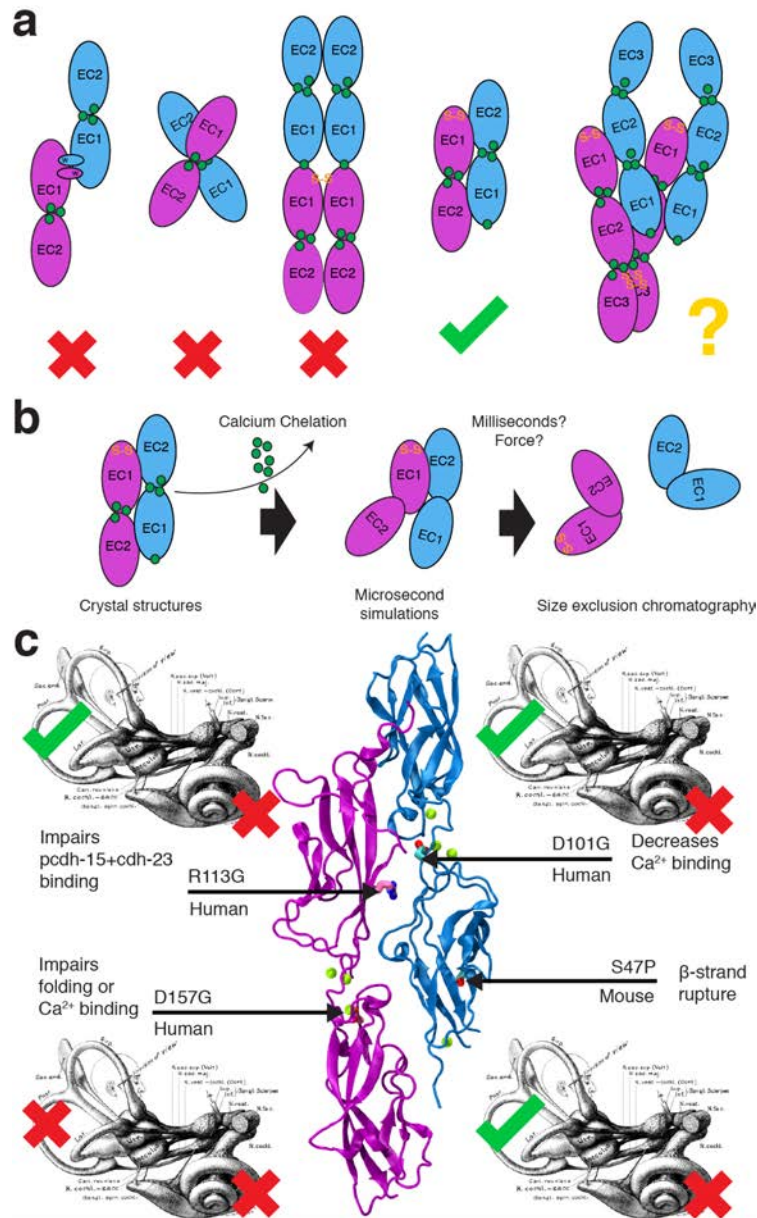
Label	Ensemble	Ion	tsim (ns)	SMD Speed (nm/ns)	Start	Size (# atoms)	Size (nm ³)
SN1	NpT	Ca ²⁺	1.1 ^a	-	-	195,123	26.6 x 9.6 x 8.1
SN2	NVE	Ca ²⁺	1.5	10	SN1		
SN3	NpT	Ca ²⁺	1.4	10	SN1		
SN4	NVE	Ca ²⁺	7.1	1	SN1		
SN5	NpT	Ca ²⁺	6.6	1	SN1		
SN6	NpT	Ca ²⁺	53.4	0.1	SN1		
SN7	NpT	Ca ²⁺	1.1 ^a	-	-	108,720	15.0 x 9.6 x 8.1
SN8	NpT	K ⁺	1.1 ^a	-	-	108,722	
SN9	NpT	Ca ²⁺	1.1 ^a	-	-	221,389	27.0 x 9.8 x 8.8
SN10	NVE	Ca ²⁺	1.5	10	SN9		
SN11	NpT	Ca ²⁺	1.5	10	SN9		
SN12	NVE	Ca ²⁺	9.5	1	SN9		
SN13	NpT	Ca ²⁺	6.3	1	SN9		
SA1	NpT	Ca ²⁺	1000.0	-	SN7	108,720	15.0 x 9.6 x 8.1
SA2	NVT	Ca ²⁺	2000.0	-	SN7		
SA3	NpT	K ⁺	1000.0	-	SN8	108,722	
SA4	NVT	K ⁺	2000.0	-	SN8		
SNA1	NpT	Ca ²⁺	5.1 ^a	-	SA1 ^b	193,446	26.6 x 9.6 x 8.1
SNA2	NVE	Ca ²⁺	1.5	10	SNA1		
SNA3	NpT	Ca ²⁺	1.5	10	SNA1		
SNA4	NVE	Ca ²⁺	10.6	1	SNA1		
SNA5	NpT	Ca ²⁺	9.8	1	SNA1		
SNA6	NpT	Ca ²⁺	78.6	0.1	SNA1		
SNA7	NpT	Ca ²⁺	336.1	0.02	SNA1		
SNA8	NpT	K ⁺	5.1 ^a	-	SA3 ^b	190,180	26.6 x 9.6 x 8.1
SNA9	NVE	K ⁺	1.5	10	SNA7		
SNA10	NpT	K ⁺	1.5	10	SNA7		
SNA11	NVE	K ⁺	13.0	1	SNA7		
SNA12	NpT	K ⁺	10.4	1	SNA7		
SNA13	NpT	K ⁺	74.6	0.1	SNA7		
SNA14	NpT	Ca ²⁺	1.1 ^a	-	SA1 ^b	377,668	26.0 x 9.5 x 16.1
SNA15	NVE	Ca ²⁺	2.0	10	SNA14		
SNA16	NpT	Ca ²⁺	1.6	10	SNA14		
SNA17	NVE	Ca ²⁺	10.3	1	SNA14		
SNA18	NpT	Ca ²⁺	9.3	1	SNA14		
SNA19	NpT	Ca ²⁺	74.3	0.1	SNA14		
SNC1	NpT	Ca ²⁺	1.1 ^a	-	-	203,769	27.8 x 9.4 x 8.2
SNC2	NVE	Ca ²⁺	1.9	10	SNC1		
SNC3	NpT	Ca ²⁺	1.8	10	SNC1		
SNC4	NVE	Ca ²⁺	8.0	1	SNC1		
SNC5	NpT	Ca ²⁺	7.4	1	SNC1		
SNC6	NpT	Ca ²⁺	69.0	0.1	SNC1		
SNC7	NpT	Ca ²⁺	257.6	0.02	SNC1		

^aThese simulations consisted of 1,000 steps of minimization, 100 ps of dynamics with the backbone of the protein restrained ($k = 1$ Kcal/mol/Å²), and the remaining time as free dynamics in the NpT ensemble ($\gamma=0.1$ ps⁻¹).

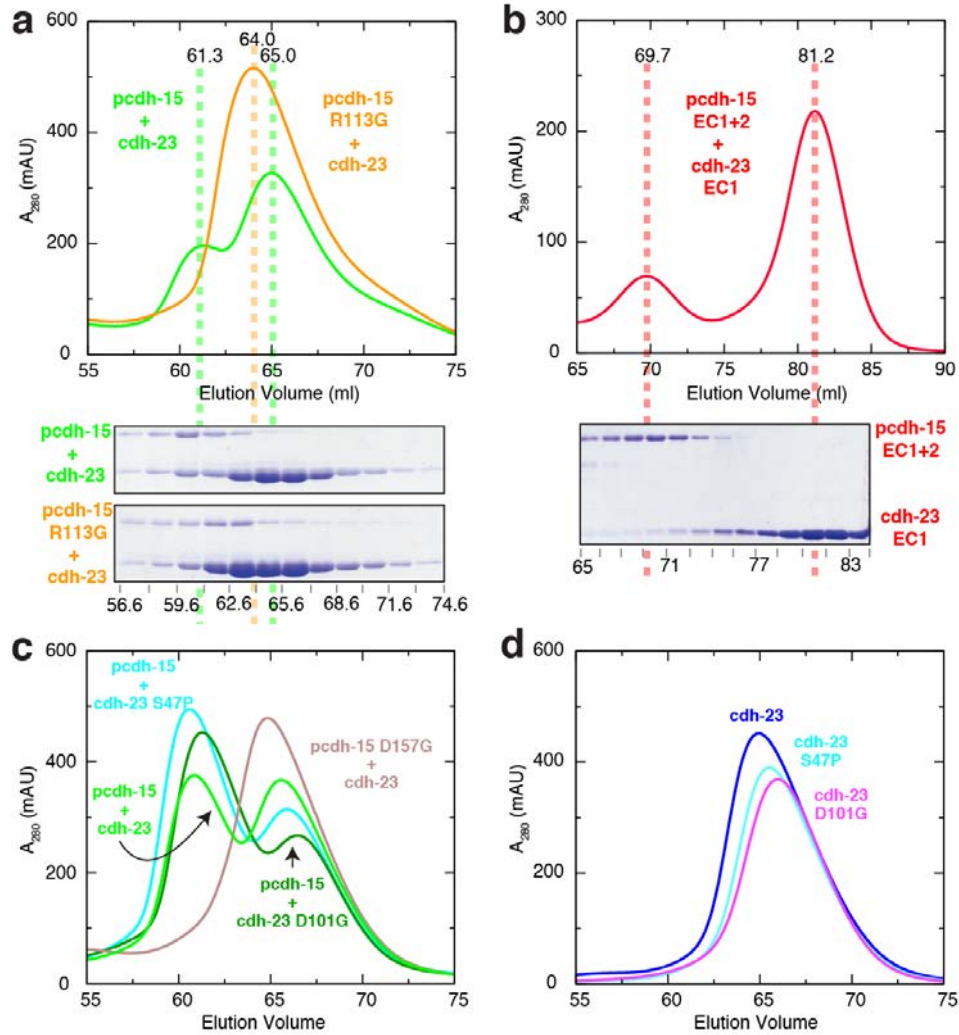
^bCoordinates of the final snapshot of SA1 or SA3 were used to build a system with a larger water box for SMD.

Summary of pcdh-15+cdh-23 and C-cadherin simulations. Labels indicate simulation platform (SN: NAMD; SA: Anton; SNA: NAMD after Anton). C-cadherin simulations are labeled SNC. Ensembles are denoted according to the thermodynamic quantities held constant (N: # atoms; p: pressure; T: temperature; V: volume; E: Energy). Occupancy of binding sites at the beginning of the simulations is indicated in Ion column. Initial coordinates and velocities (when applicable) were obtained from the last frame of the simulations indicated in the Start column. Initial size of the system (in nm³) is indicated in the last column. All pcdh-15+cdh-23 simulations used structure S1b, except for simulations SN9 to SN13, which used structure S1a.

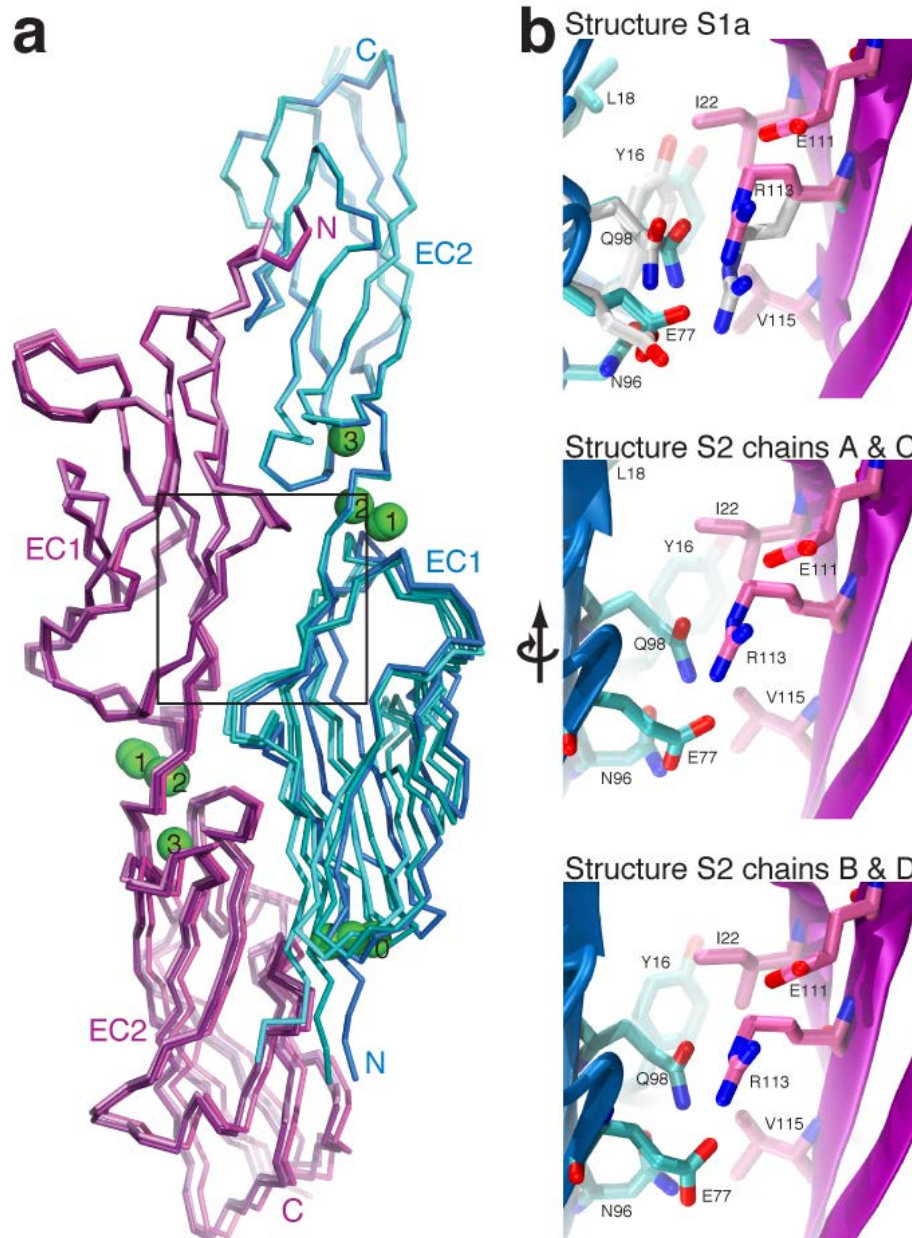
Supplementary Figures and Legends



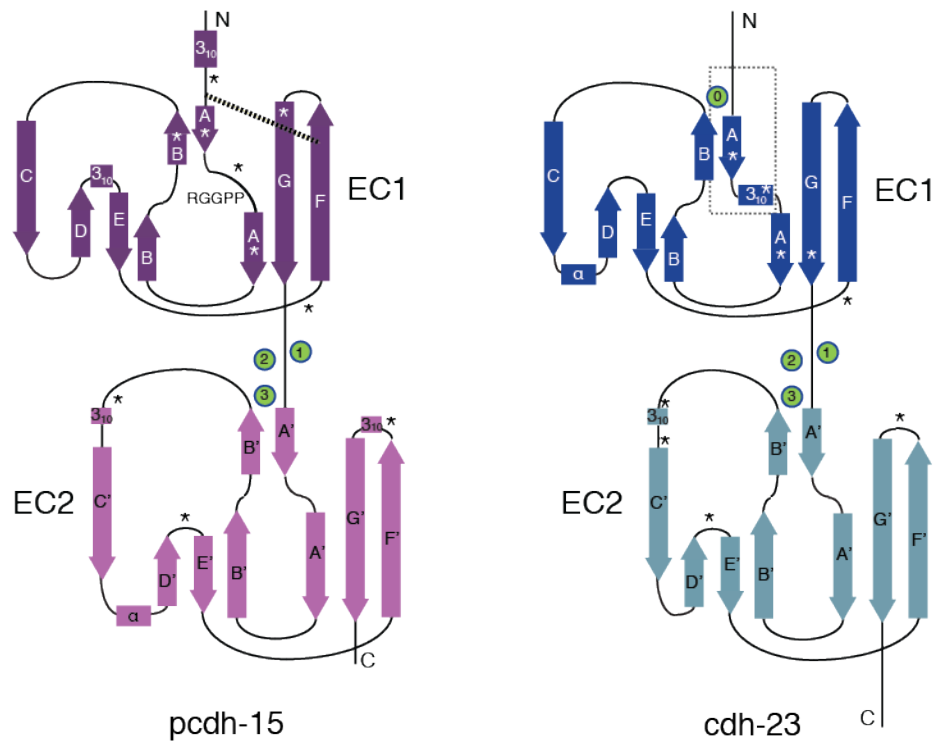
Supplementary Figure 1. Structural determinants of tip-link function in hearing and deafness. **a**, The bond formed by protocadherin-15 and cadherin-23 does not involve β -strand exchange or formation of an X-dimer as in classical cadherins^{50,68-70}, and is not directly mediated by Ca^{2+} as previously suggested^{16,17}. An overlapped antiparallel dimer involving the N-terminal EC1+2 repeats of each protein forms the protocadherin-15 and cadherin-23 bond. Parallel homodimerization is likely mediated by other repeats beyond EC2 in each protein. **b**, Ca^{2+} chelation promotes disassembly of the pcdh-15+cdh-23 bond, as determined by SEC experiments. Microsecond-long molecular dynamics simulations suggest that removal of Ca^{2+} results in entropic stress, which may lead to complex separation over a longer time scale or may facilitate disassembly by mechanical force. A transient, Ca^{2+} -free complex is predicted to exist. **c**, Deafness-related mutations are located in the pcdh-15+cdh-23 structure. Known phenotype (auditory and/or vestibular) is indicated along with structural defects suggested by our biochemical experiments, presented here and in ref 16.



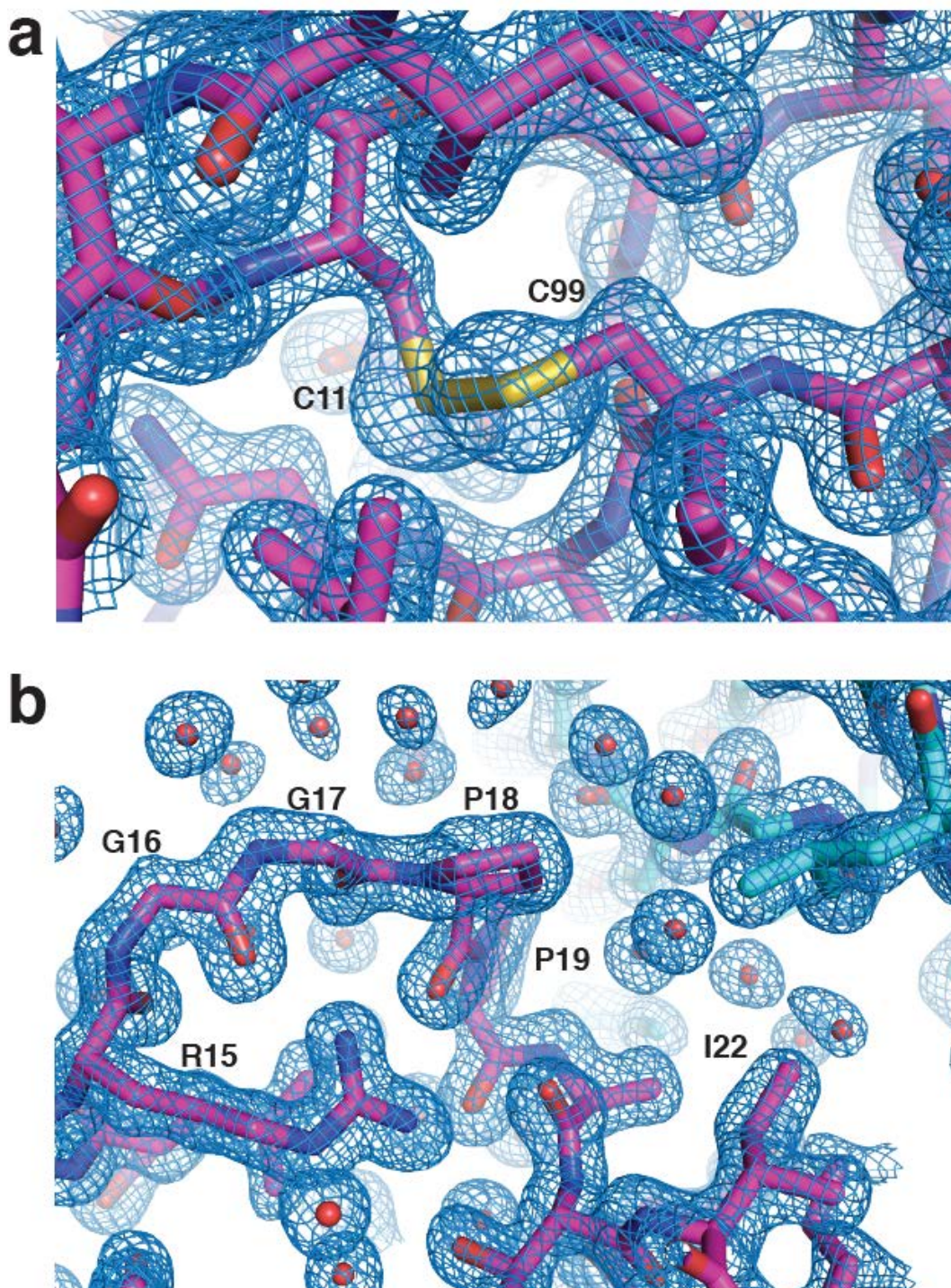
Supplementary Figure 2. SEC of co-refolded protocadherin-15 and cadherin-23 fragments. **a**, Representative traces for wild-type protocadherin-15 EC1+2 co-refolded with cadherin-23 EC1+2 (pcdh-15+cdh-23, green), and mutant pcdh-15_{R113G} co-refolded with cdh-23 (pcdh-15_{R113G}+cdh-23, orange). Experiments were performed using a Superdex S75 16/60 column. Coomassie-stained SDS-PAGE analysis of eluted fractions is shown below the chromatogram. Trace for co-refolded pcdh-15+cdh-23 (green) shows two peaks; the first one, at 61.3 ml, contained both proteins (complex) and was used for crystallization. The second peak (65 ml) contained cdh-23 alone. Trace for co-refolded pcdh-15_{R113G}+cdh-23 shows a single peak with no obvious shift in elution volume for protein fragments. **b**, Representative trace for wild-type pcdh-15 co-refolded with cadherin-23 EC1 (red). The two protein fragments eluted independently from each other in two peaks (69.7 ml and 81.2 ml) as indicated by Coomassie-stained SDS-PAGE of the eluted fractions shown beneath the chromatogram. Similar results were obtained for pcdh-15_{R113G} and pcdh-15_{I22A}. Fractions from the first peak were used for further SEC or ITC (Figs 2 & 4). **c**, SEC of co-refolded wild-type pcdh-15+cdh-23 and mutants involved in inherited deafness. Traces indicate that mutations D101G and S47P in cdh-23 did not prevent complex formation. SEC of co-refolded pcdh-15_{D157G} + cdh-23 shows a single peak with negligible amounts of pcdh-15_{D157G}. **d**, SEC traces of refolded wild-type cdh-23 and mutants show single monodisperse peaks for all samples. All SEC experiments in this figure were performed in the presence of 1 mM CaCl₂.



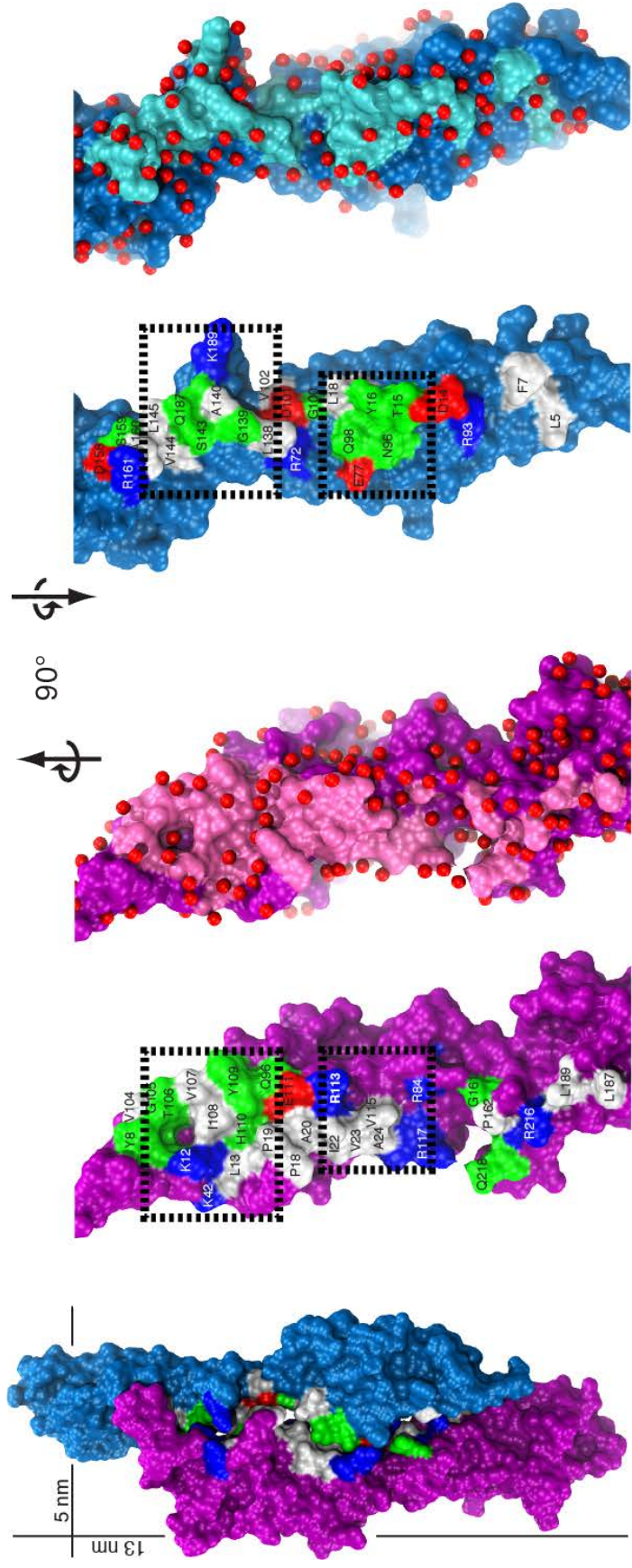
Supplementary Figure 3. Pcdh-15+cdh-23 structures showed nearly identical conformations for individual pcdh-15 and cdh-23 fragments with flexing at the linker regions (up to $\sim 10^\circ$). **a**, Superposition of the S1a structure (darker colors) and the two complexes in the asymmetric unit of the S2 structure. The three structures were superimposed on the cdh-23 EC2 repeat to highlight the slight linker flexibility that results in mostly coordinated displacement of the EC1 repeat of cdh-23 and the EC2 repeat of pcdh-15. The buried surface area of the three complexes is 907 \AA^2 for S1a, 1069 \AA^2 for S2 chains A and C, and 1160 \AA^2 for S2 chains B and D. The three structures are shown as C α traces, with pcdh-15 in purple, cdh-23 in blue and Ca²⁺ ions as green spheres. Box indicates the approximate position of the detail shown in (b). **b**, Detail of interface between pcdh-15 and cdh-23 for the three structures superimposed in (a). This region of the interface is centered on residue R113, which when mutated causes deafness. Protein backbone and surrounding residues are shown in cartoon (pcdh-15, purple; cdh-23, blue) and sticks (pcdh-15, pink; cdh-23, cyan). In the top panel, the high-resolution structure showed alternative conformations for a few sidechains, shown in gray.



Supplementary Figure 4. Topology diagrams for pcdh-15 and cdh-23. Protocadherin-15 repeats EC1 and EC2 feature typical cadherin folds with seven β -strands labeled A to G. Pcdh-15 EC1 features a 3_{10} helix and the C11-C99 disulfide bond (dashed line) linking β -strands F and A at the N-terminus. Regions involved in heterophilic interactions are indicated with an asterisk (*).



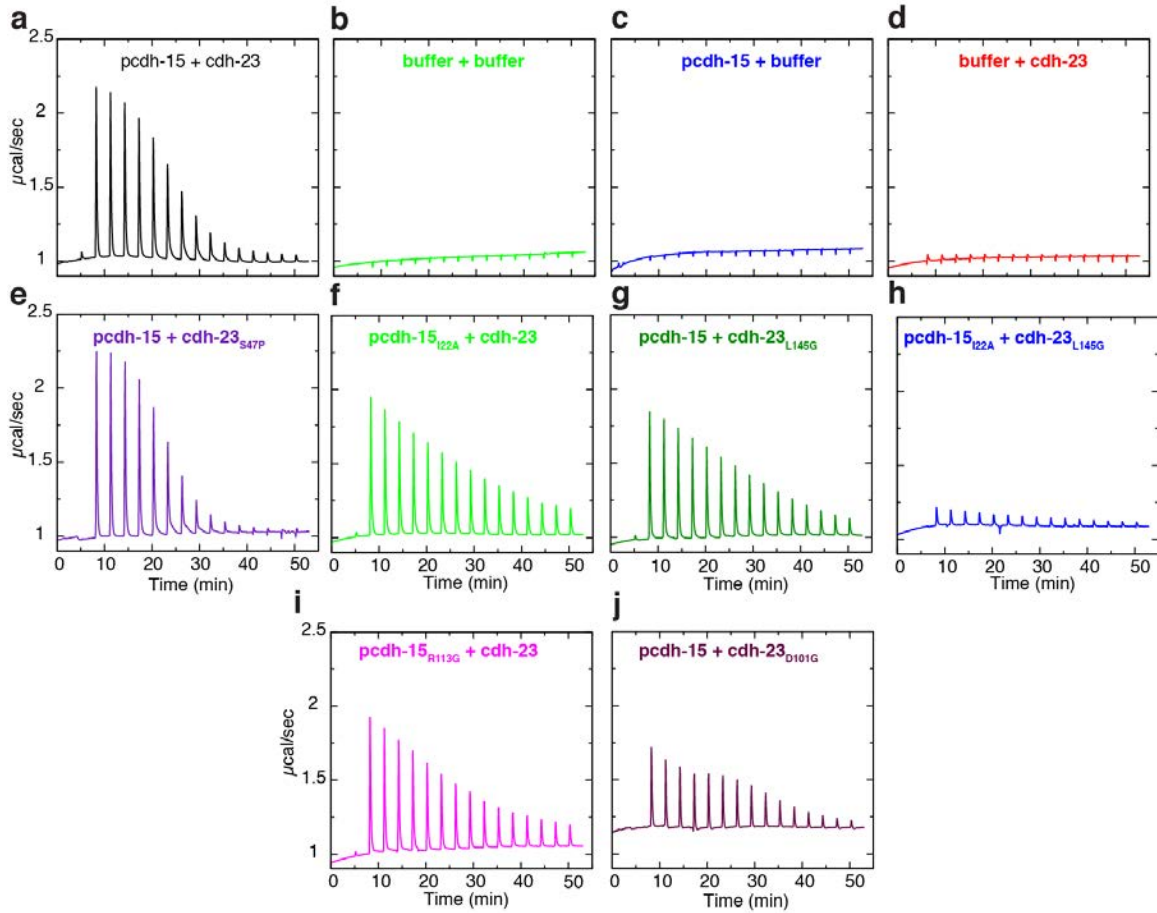
Supplementary Figure 5. Unique structural features of pcdh-15. Weighted $2F_o - F_c$ electron density map from the S1a structure contoured at 1.5σ . **a**, The disulfide bond linking C11 and C99 clamps the N-terminal end of the EC1 β -sandwich. **b**, The RXGPP loop is buttressed by interactions of the arginine sidechain with the carbonyl groups of both prolines. Pcdh-15 is shown in magenta and cdh-23 in cyan.



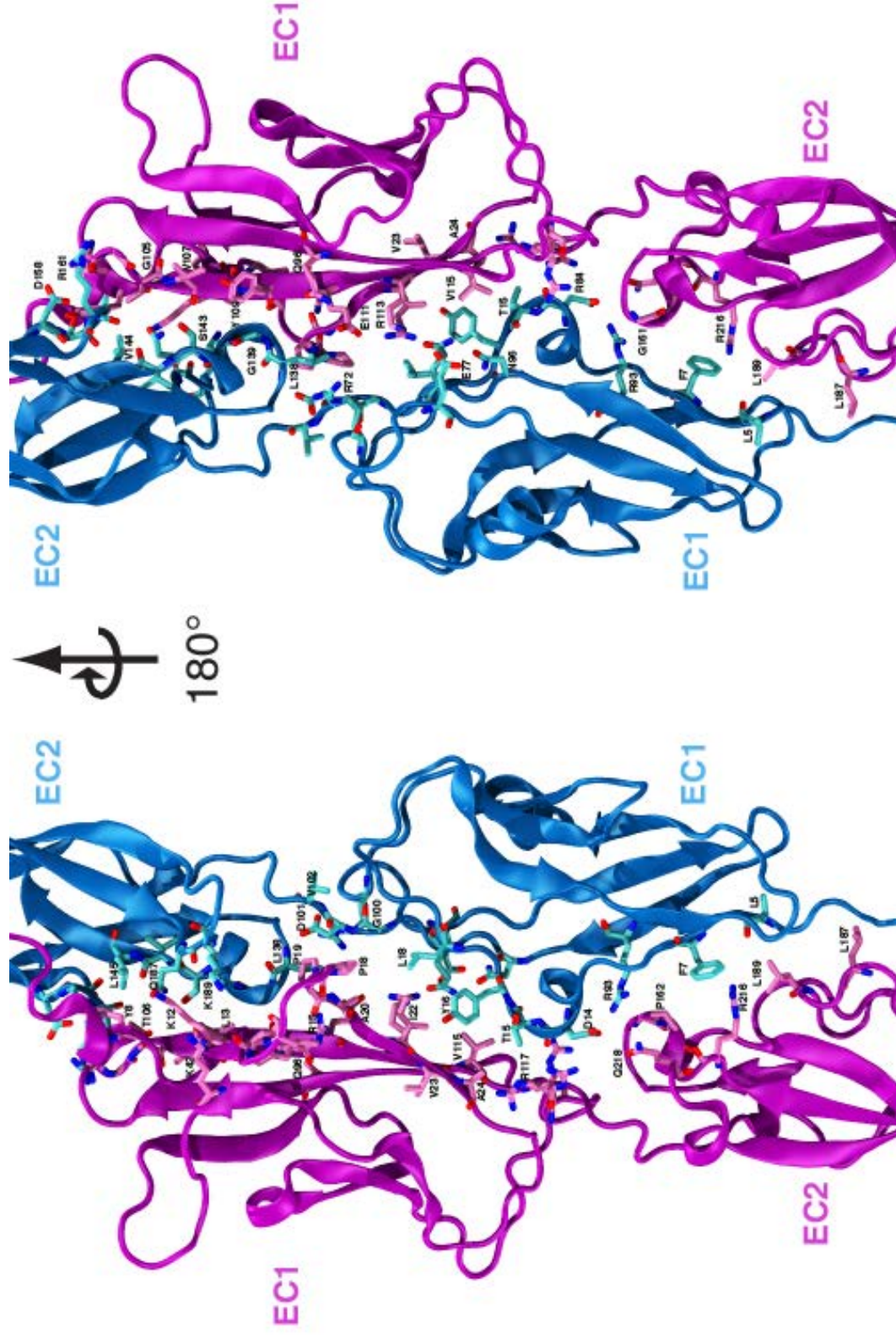
Supplementary Figure 6. Features of the pcdh-15+cdh-23 interface. Molecular surface representation of pcdh-15 (purple) and cdh-23 (blue). The interaction surfaces are also exposed with interfacing residues labeled and colored according to residue type (white: apolar; green: polar; red: negatively charged; blue: positively charged). Water molecules (red spheres) within 3 Å of each protomer are shown with interfacing residues colored in pink (pcdh-15) and cyan (cdh-23). Dashed boxes indicate the two main areas of interaction.



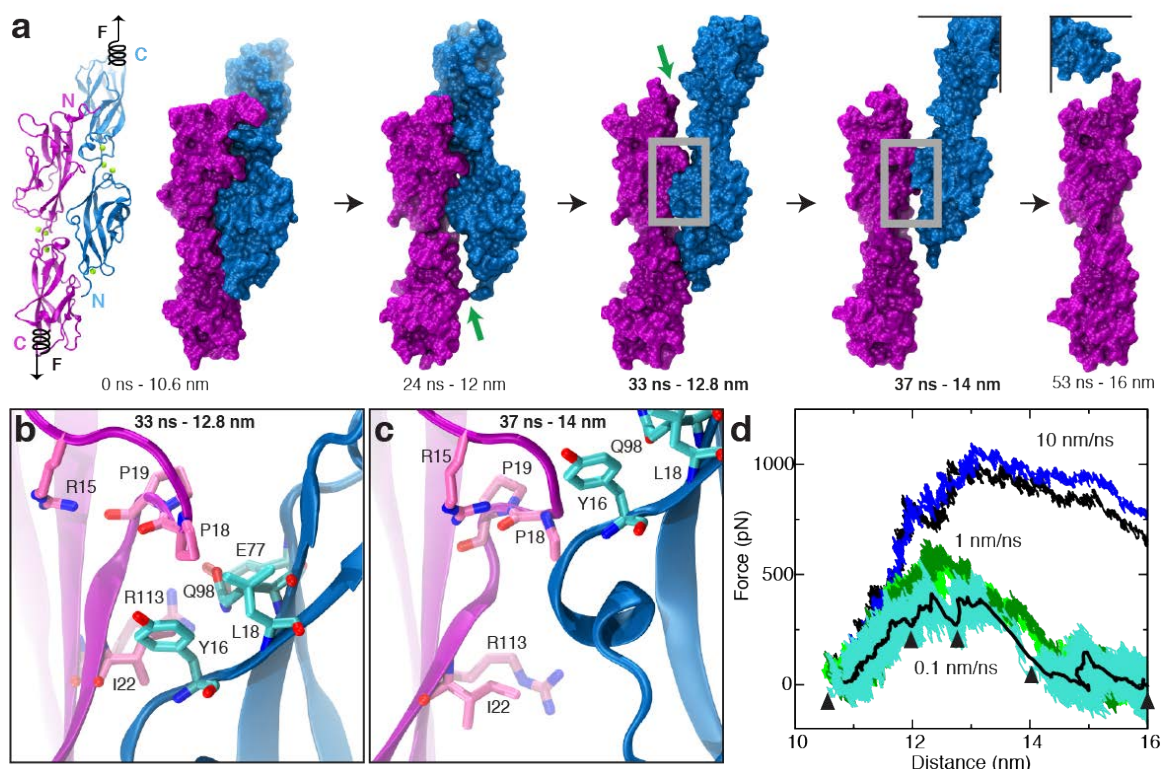
Supplementary Figure 7. Alignment of cadherin-23 and protocadherin-15 sequences for repeats EC1 (top) and EC2 (bottom) corresponding to *Mus musculus* (Mm), *Homo sapiens* (Hs), and *Gallus gallus* (Gg). NCBI reference sequences: NP_075859.2, NP_071407.4, XP_421595.2; NP_001136218.1, NP_001136235.1, NP_001038119.1. Conserved Ca²⁺-binding motifs are labeled XEX^{BASE}, DXD, DRE, XDX^{TOP}, and DXNDN. Black arrowheads indicate differences between *Mus musculus* and *Homo sapiens* sequences. Interfacing residues are indicated with an asterisk (*). Blue and red arrowheads indicate predicted O- and N-glycosylation sites. Secondary structure is indicated below the alignment for each protein.



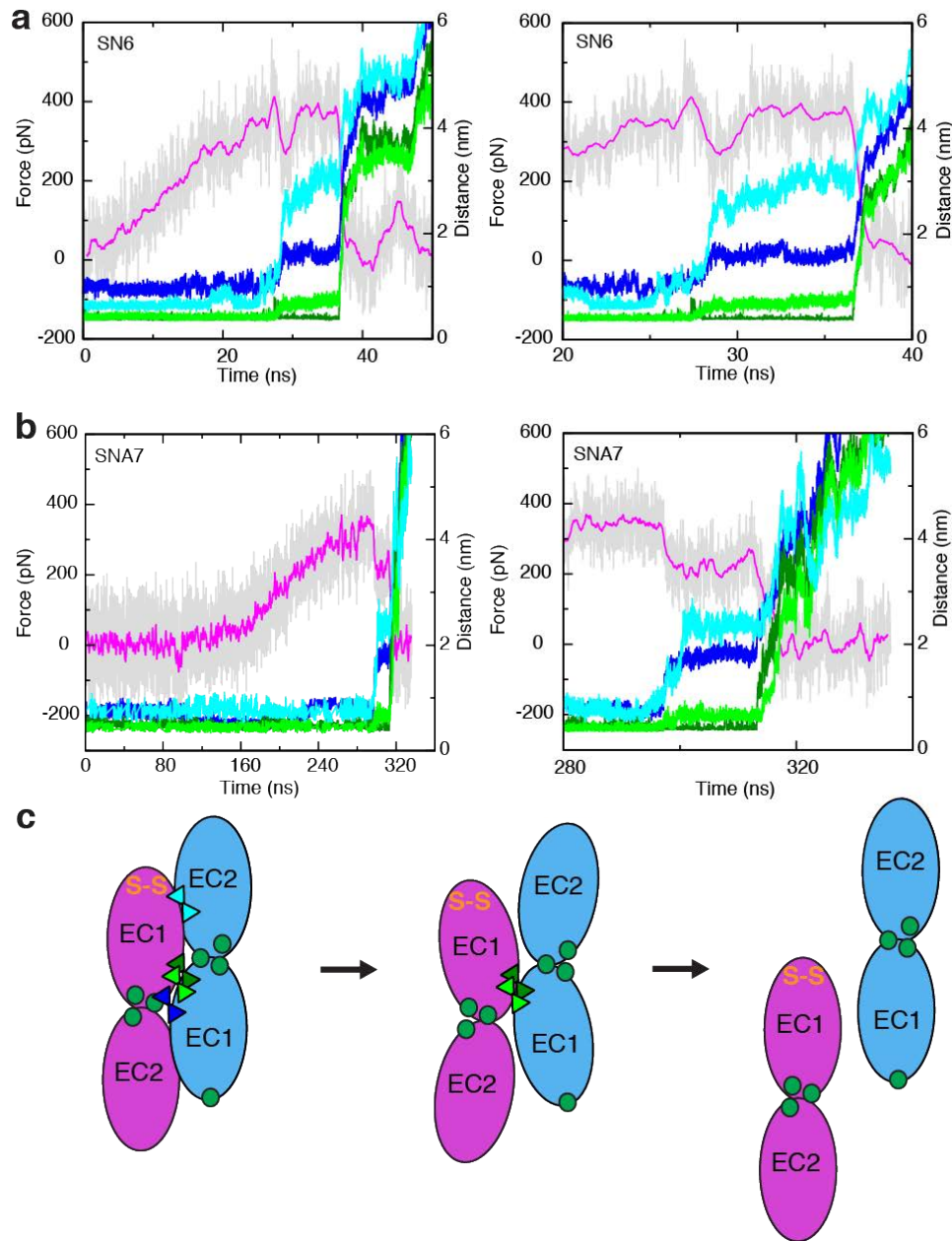
Supplementary Figure 8. Pcdh-15+cdh-23 complex formation probed using isothermal titration calorimetry (ITC) and site-directed mutagenesis. Raw power vs time data are shown for: **a**, pcdh-15 (111 μM) titrated with cdh-23 (1.1 mM, same as in Fig. 2a); **b**, buffer titrated with buffer (control); **c**, pcdh-15 (111 μM) titrated with buffer (control); **d**, buffer titrated with cdh-23 (1.1 mM, blank); **e**, pcdh-15 (120 μM) titrated with cdh-23_{S47P} (1.2 mM); **f**, pcdh-15_{I22A} (110 μM) titrated with cdh-23 (1.1 mM); **g**, pcdh-15 (130 μM) titrated with cdh-23_{L145G} (1.2 mM); **h**, pcdh-15_{I22A} (114 μM) titrated with cdh-23_{L145G} (1.2 mM, same as in Fig. 2a); **i**, pcdh-15_{R113G} (110 μM) titrated with cdh-23 (1.1 mM); **j**, pcdh-15 (156 μM) titrated with cdh-23_{D101G} (1.2 mM). All experiments were performed at 10°C with matched buffers.



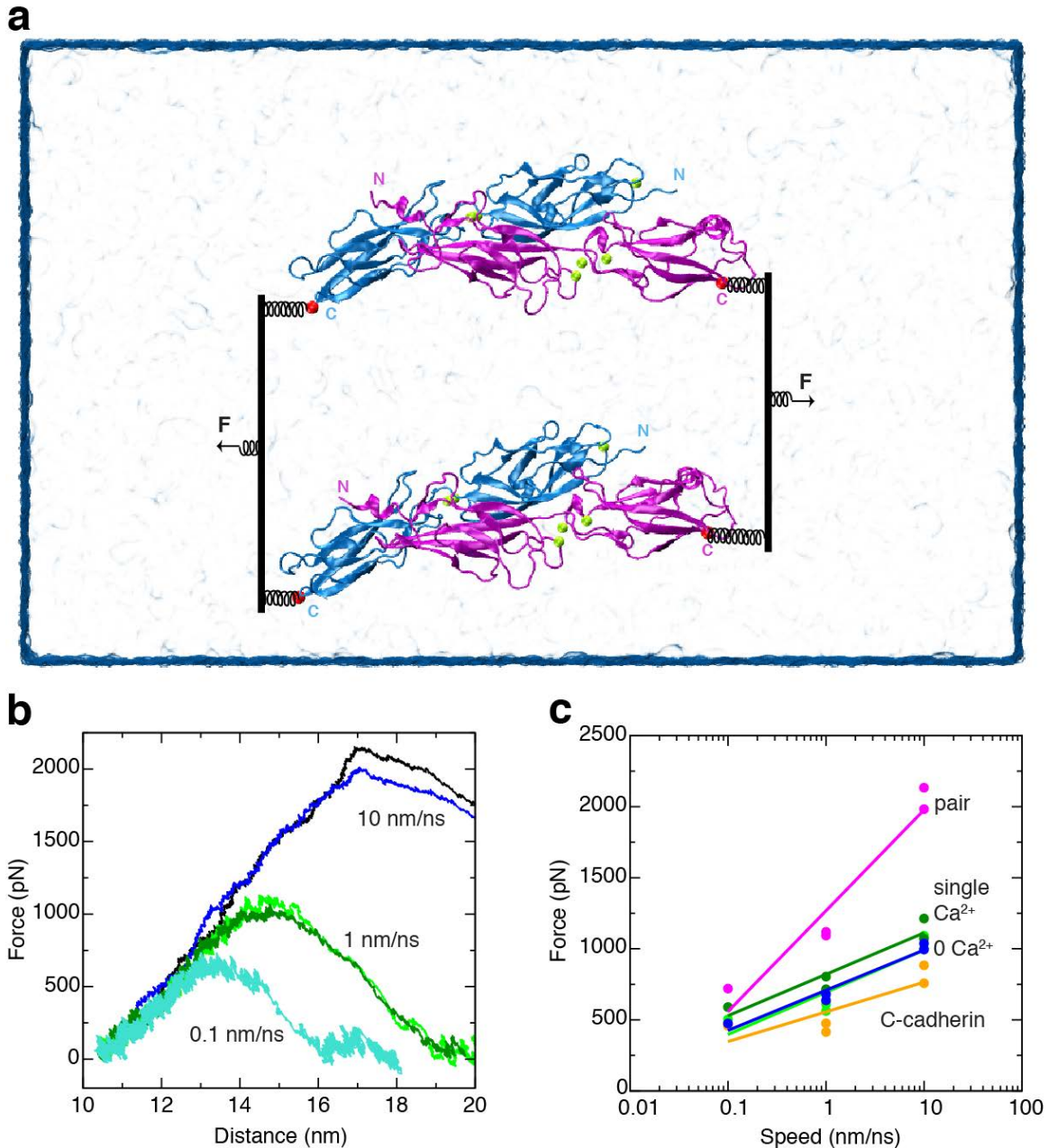
Supplementary Figure 9. Details of the pcdh-15+cdh-23 interface. Two views of a ribbon diagram of pcdh-15 (purple) and cdh-23 (blue) with interfacing residues labeled and shown in stick representation.



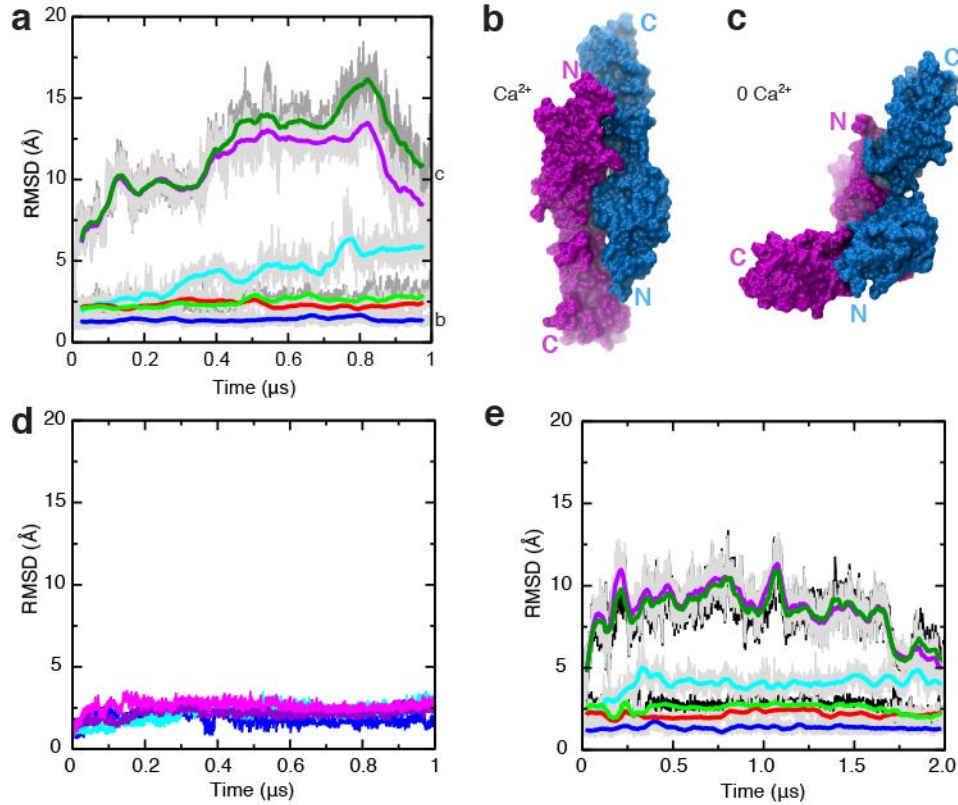
Supplementary Figure 10. Mechanical strength of the pcdh-15+cdh-23 complex probed by SMD simulations. **a**, Snapshots of pcdh-15 (purple) and cdh-23 (blue) unbinding during simulation SN6 (Supplementary Table 3). The protein complex is shown in both cartoon and surface representations at the beginning of the simulation, and then in surface representation at indicated time points. Ca^{2+} ions are shown as green spheres. Force was applied to the C-termini of both protomers. Complete complex separation was achieved after 50 ns. Green arrows point to broken interfaces; gray boxes are detailed in **b-c**, showing interacting residues before and after sliding during unbinding. **d**, Force applied to one C-terminus versus distance between C-termini ends of pcdh-15 and cdh-23. Different traces correspond to independent simulations performed at stretching speeds of 10 (blue and black), 1 (light and dark green), and 0.1 nm/ns (cyan). Snapshots in (a) are indicated by arrowheads. A 1-ns running average of the cyan curve is shown in black. At least one clear unbinding force peak was discernable in each simulation.



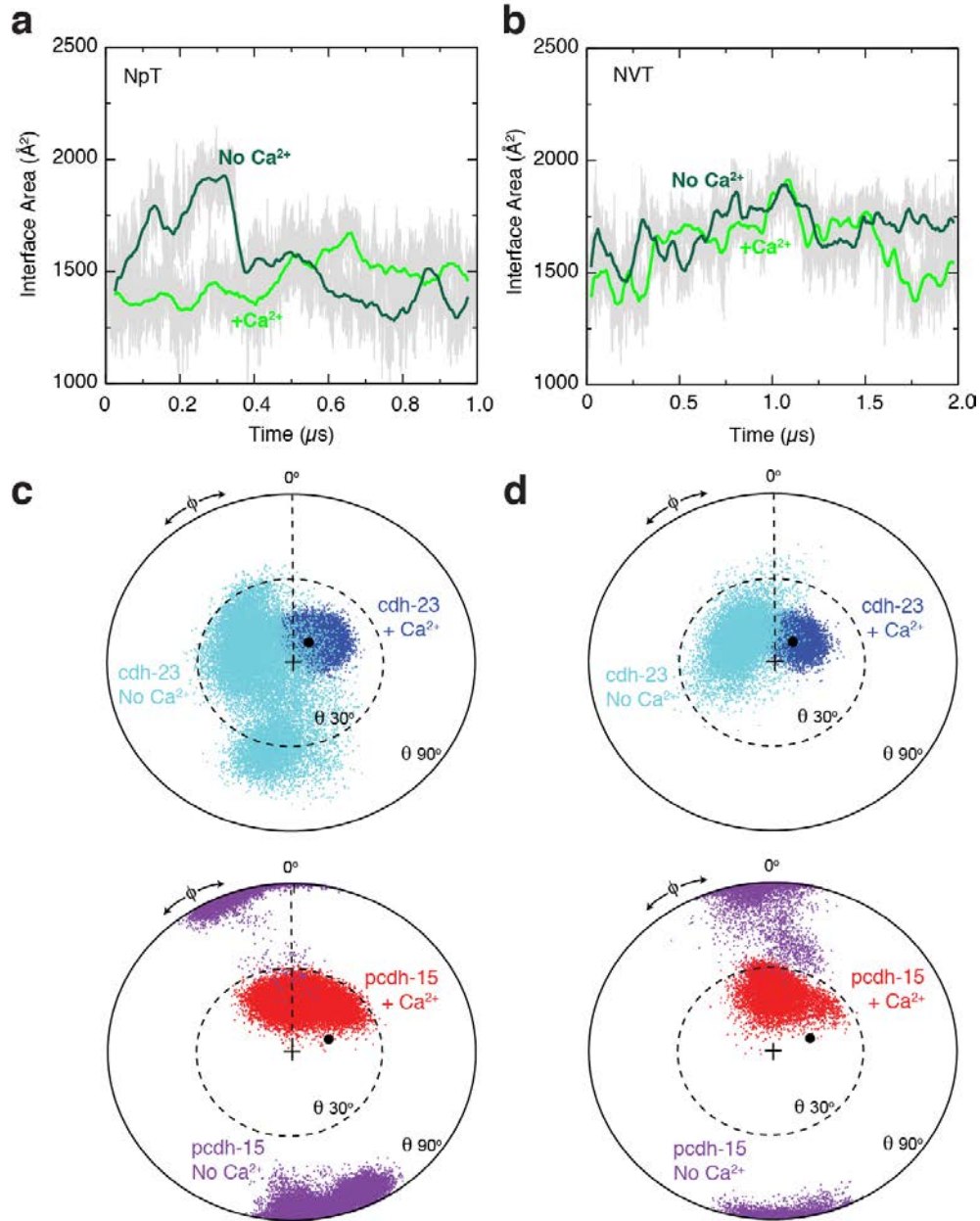
Supplementary Figure 11. Molecular correlates of pcdh-15+cdh-23 forced unbinding. **a-b**, Force (left scale) applied to one of the protein complex C-termini along with distances between residues versus time for simulations SN6 and SNA7, respectively. Force is shown in gray, with 1-ns running average in magenta. Distances (right scale) were monitored throughout SMD simulations at four locations: the tip of pcdh-15 and the adjacent EC2 repeat of cdh-23 (pcdh-15_{T106}C_β – cdh-23_{L145}C_γ in cyan); the center of the interface (pcdh-15_{R113}C_ε – cdh-23_{E77}C_ε in dark green and pcdh-15_{I22}C_β – cdh-23_{Y16}C_ε in light green); and the EC1 repeat of cdh-23 and the adjacent residues in pcdh-15 (pcdh-15_{R84}C_ε – cdh-23_{N96}C_γ in blue). Right panels show detail during unbinding, highlighting a sequential separation with detachment of bonds in green occurring last. **c**, Schematic location of bonds described in (a) and (b) throughout forced unbinding.



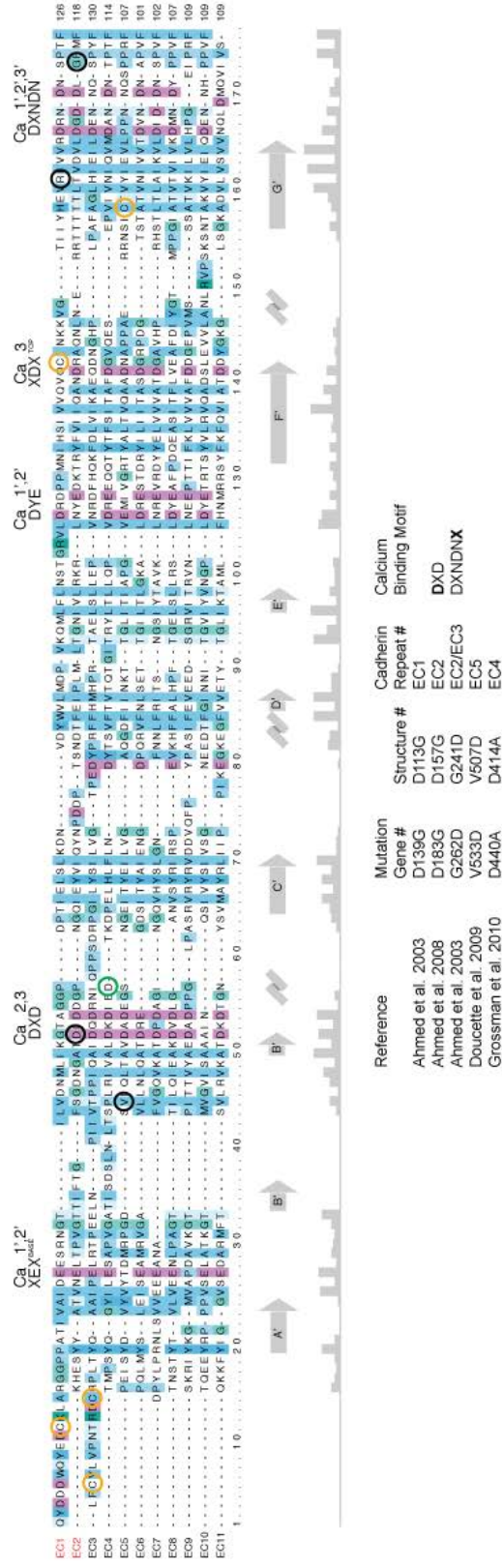
Supplementary Figure 12. Mechanical strength of two pcdh-15+cdh-23 complexes in parallel. **a**, System setup. Two pcdh-15+cdh-23 complexes were placed in parallel but far from each other in a large water box. The C-termini of the two pcdh-15 protomers were connected to a virtual slab through independent springs with spring constants equivalent to two EC repeats each. The slab was in turn connected to an SMD atom moving at constant velocity (all forces were applied in the stretching direction only). A similar arrangement was set for the C-termini of cdh-23. **b**, Force applied to one of the slabs versus distance between slabs. Different traces correspond to independent simulations performed at stretching speeds of 10 (blue and black), 1 (light and dark green), and 0.1 nm/ns (cyan). **c**, Maximum force-peak values vs. stretching speed for unbinding simulations of the pair of complexes shown in magenta (simulations SNA15 to SNA19). Unbinding force-peak values for simulations of single complexes with (green) and without Ca^{2+} (blue), as well as for C-cadherin (SNC2 to SNC6, orange) are shown for reference.



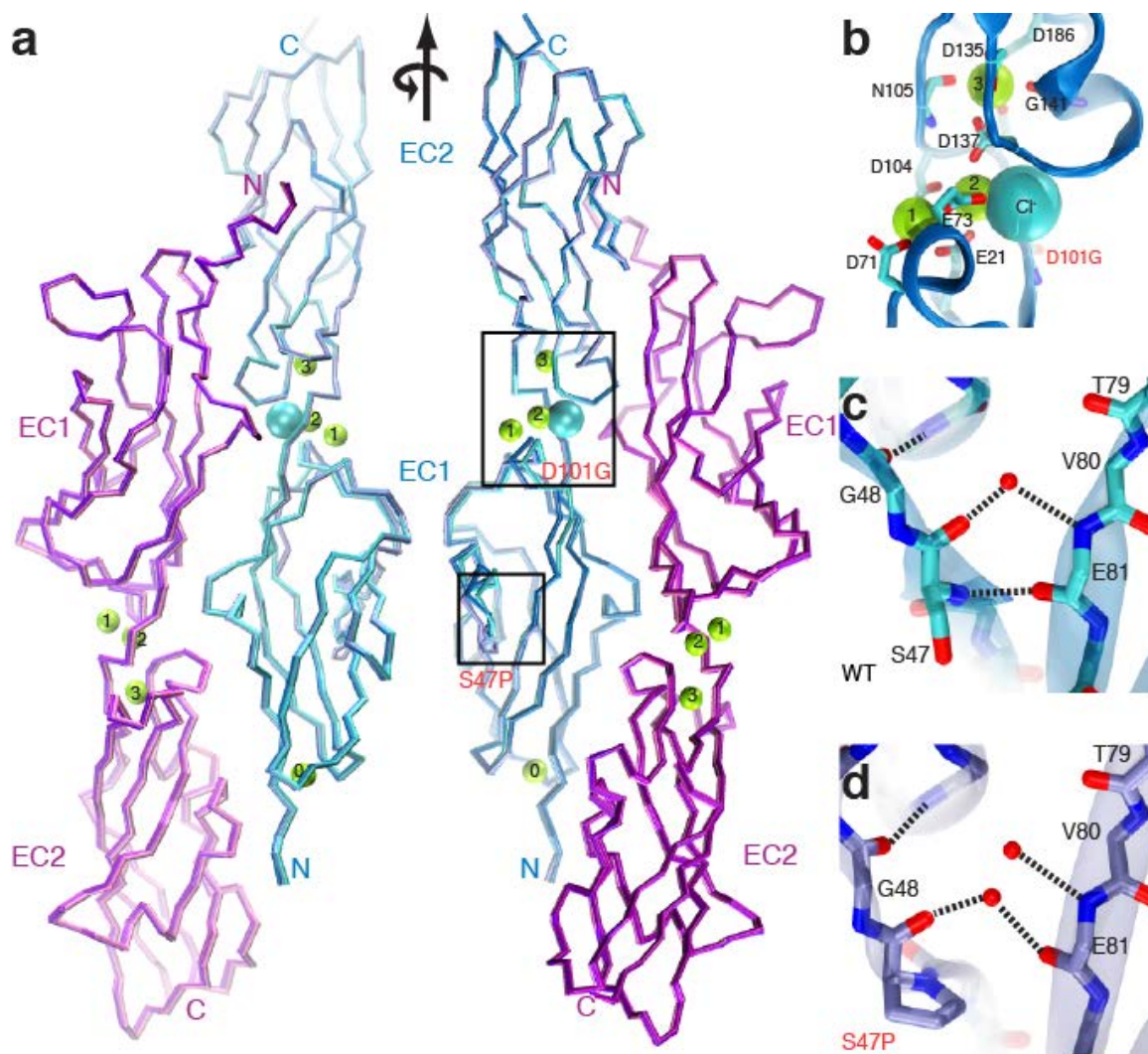
Supplementary Figure 13. Removal of bound Ca^{2+} causes complex instability in simulations. **a**, RMSD versus time for simulations SA1 and SA3 in the NpT ensemble (Supplementary Table 3) of the cdh-23+pcdh-15 complex in the presence (light green, whole complex; red, pcdh-15; blue, cdh-23) and the absence of bound Ca^{2+} (dark green, whole complex; magenta, pcdh-15; cyan, cdh-23). **b-c**, Snapshots of the pcdh-15+cdh-23 complex at the end of simulations performed with and without bound Ca^{2+} , respectively. See Supplementary Movies III, IV&V. **d**, Stability of individual EC repeats. RMSD per repeat versus time for simulation of the cdh-23+pcdh-15 complex in the absence of bound Ca^{2+} (SA3; cadherin-23 EC1, blue; cadherin-23 EC2, cyan; protocadherin-15 EC1, violet; protocadherin-15 EC2, magenta). While the complex deformed, individual repeats retained their fold. **e**, RMSD versus time for simulations SA2 and SA4 in the NVT ensemble, shown as in (a).



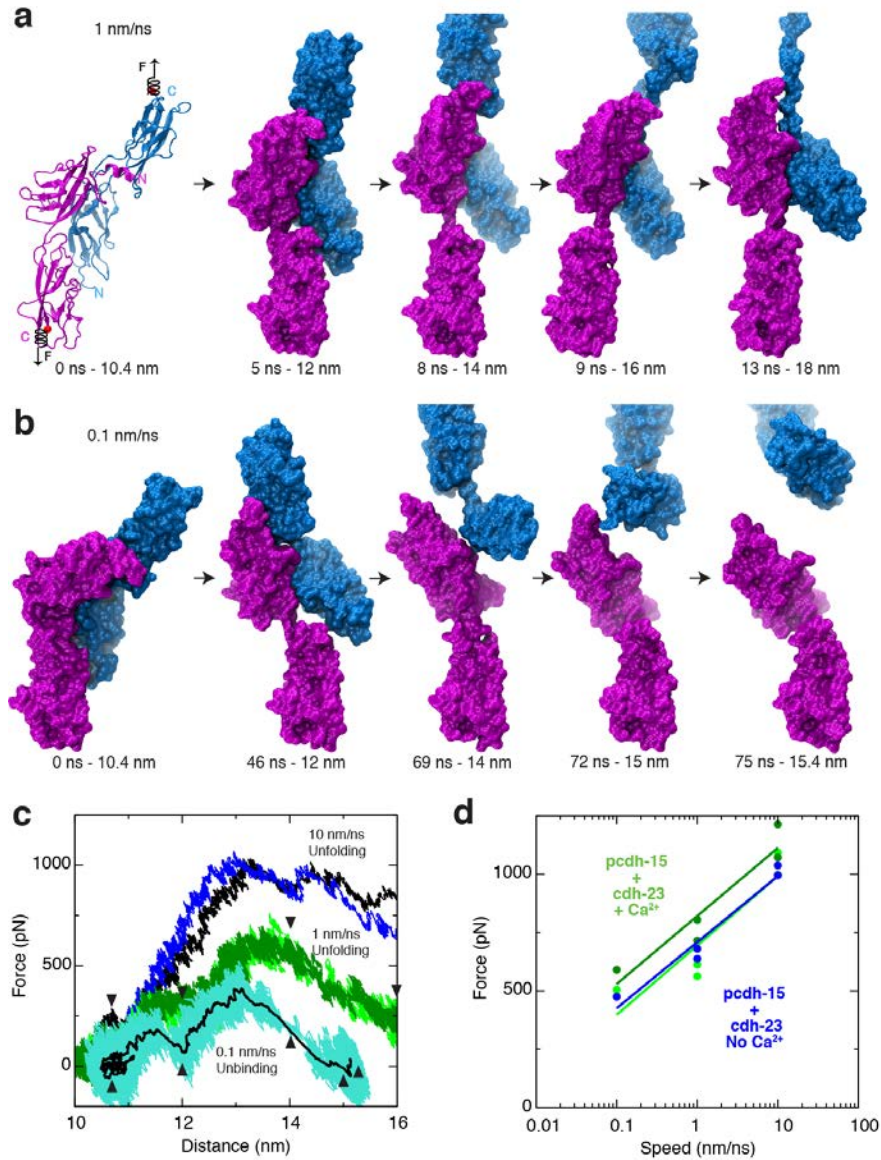
Supplementary Figure 14. Interface area and interrepeat arrangement during simulations with and without bound Ca^{2+} . **a-b**, Surface area of the pcdh-15+cdh-23 interface shown for simulations performed with (light green) and without bound Ca^{2+} (dark green). Simulations SA1 and SA3 in the NpT ensemble are shown in (a), simulations SA2 and SA4 in the NVT ensemble are shown in (b). **c-d**, Conformational freedom of EC2 with respect to EC1 quantified by the projection of the EC2 principal axis into the x-y plane perpendicular to the EC1 principal axis¹⁶. Vector length relates to the tilt angle ($\sin \theta$), while the phase angle corresponds to the azimuthal angle ϕ . Projections are shown for the cdh-23 protomer in the presence (blue) and absence of bound Ca^{2+} (cyan) for simulations SA1 and SA3 (c), as well as simulations SA2 and SA4 (d). Similarly, projections are shown for the pcdh-15 protomer in the presence (red) and absence of bound Ca^{2+} (violet). Black circles highlight initial projections. Both cdh-23 and pcdh-15 display a dramatic increase in inter-repeat motion upon Ca^{2+} removal.



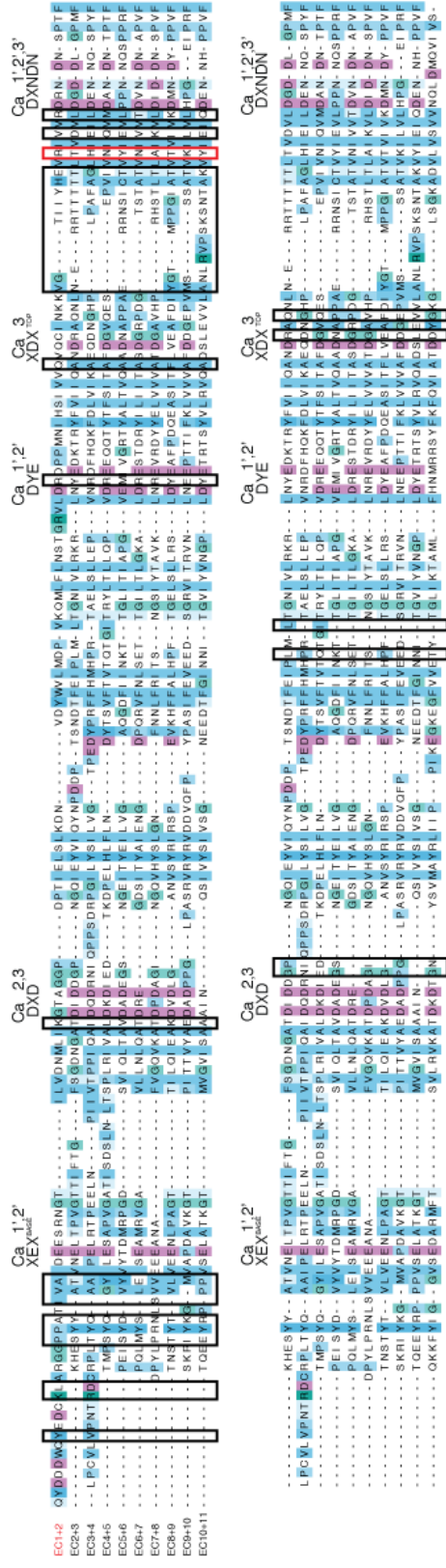
Supplementary Figure 15. Extracellular repeats of human protocadherin-15 and mutations causing hereditary deafness. All 11 extracellular repeats are aligned to each other (EC1 to EC11). Conserved Ca²⁺-binding sequence motifs are labeled as in Supplementary Fig. 7. Mutations causing hereditary deafness are mapped onto the sequence alignment (top) and listed (bottom) along with their repeat location, reference^{27,71,72}, and Ca²⁺-binding motif target. A variant positively selected in East Asians is highlighted in green⁶⁷. Cysteine residues are highlighted in yellow. Secondary structure of protocadherin-15 EC2 and sequence conservation are indicated in gray below the alignment.



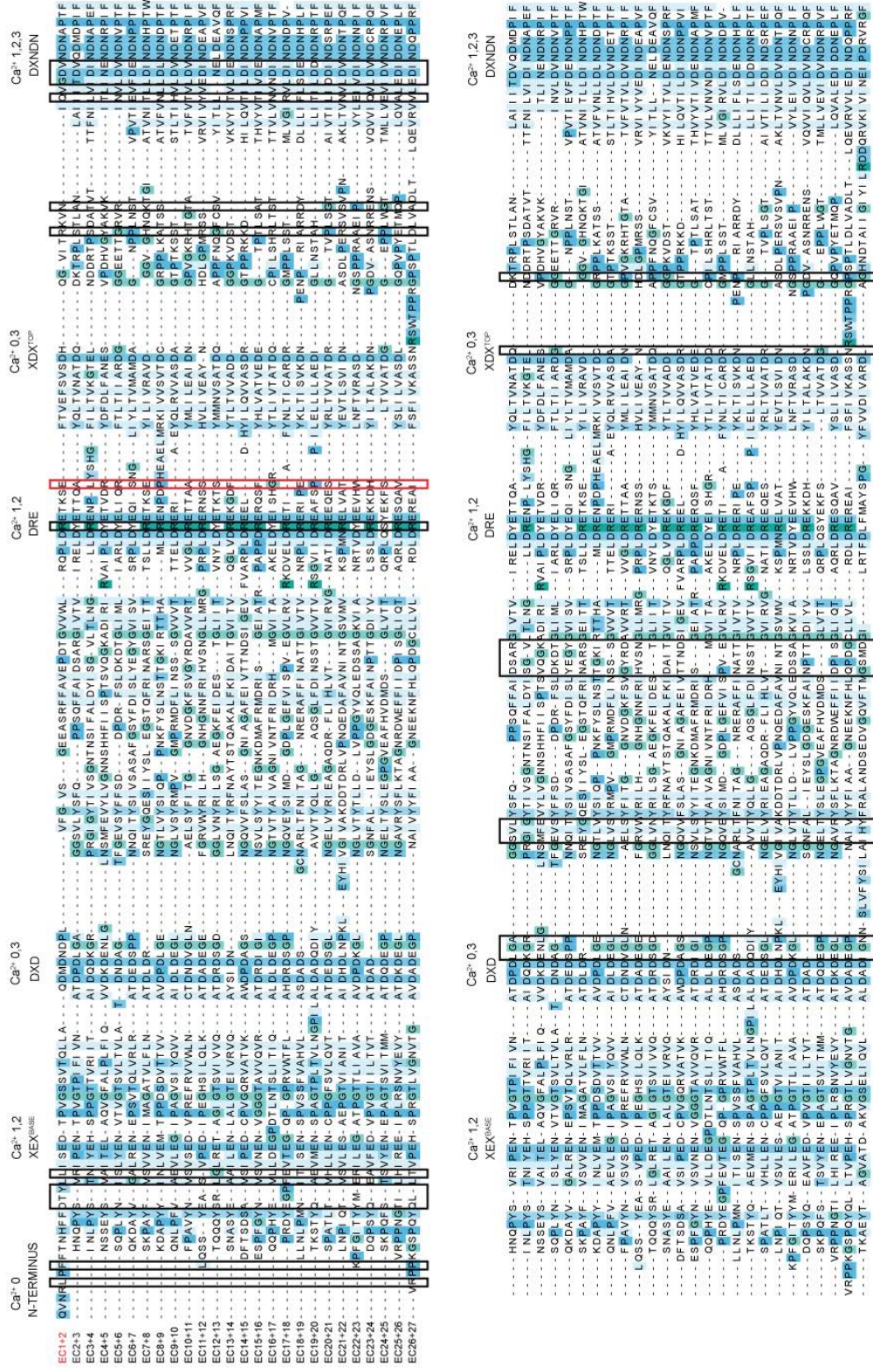
Supplementary Figure 16. Structures of mutant pcdh-15+cdh-23 complexes. **a**, Two views of a superposition of the S1a structure (darker colors) and the two mutant complexes involving cdh-23_{D101G} (S3, cyan) and cdh-23_{S47P} (S4, ice-blue). The three structures were superimposed on the cdh-23 EC2 repeat and shown as C_α traces, with pcdh-15 in purple and cdh-23 in blue. One Cl⁻ and seven Ca²⁺ ions are shown as cyan and green spheres, respectively. Boxes indicate the approximate position of the details shown in (b-d). **b**, Detail of the cdh-23_{D101G} linker region, with a Cl⁻ ion bound to Ca²⁺ at binding-site 2¹⁶. **c-d**, Detail of interactions between EC1 β-strands C and F for wild-type cdh-23 (S1a) and the cdh-23_{S47P} mutant (S4), respectively. The cyclic side-chain of P47 prevents the formation of a hydrogen bond with the carbonyl oxygen of E81, favoring the separation of both strands by an additional water molecule. Protein backbone and surrounding residues are shown in sticks (cdh-23, cyan; pcdh-15, ice-blue).



Supplementary Figure 17. Mechanical strength of the pcdh-15+cdh-23 complex probed in the absence of bound Ca^{2+} . **a**, Snapshots of pcdh-15 (purple) and cdh-23 (blue) during simulation SNA11 performed using a stretching speed of 1 nm/ns (Supplementary Table 3). The protein is shown in cartoon representation at the beginning of the simulation, and then in surface representation at indicated time points. The second repeat of cdh-23 unfolded before unbinding of the complex could be observed. **b**, Snapshots of pcdh-15 and cdh-23 as in (a) during simulation SNA13 performed using a stretching speed of 0.1 nm/ns. Complete complex separation was achieved after 70 ns and was preceded by inter-repeat extension (linker unfolding). **c**, Force applied to one C-terminus versus distance between C-termini ends of pcdh-15 and cdh-23. Different traces correspond to independent simulations performed at stretching speeds of 10 (blue and black), 1 (light and dark green), and 0.1 nm/ns (cyan). Snapshots in (a) and (b) are indicated by arrowheads pointing down and up, respectively. A 1-ns running average of the cyan curve is shown in black. Unfolding of an EC repeat preceded unbinding in all simulations except the slowest one. **d**, Maximum force-peak values vs. stretching speed for simulations of the pcdh-15+cdh-23 complex in the absence of bound Ca^{2+} are shown in blue (simulations SNA9 to SNA13). Unbinding forces for simulations with Ca^{2+} (Fig. 3d) are shown in green.



Supplementary Figure 18. Extracellular repeats of human protocadherin-15 and binding interface. All 10 extracellular pairs of repeats are aligned to each other (EC1+2 to EC10+11). Boxes indicate interfacing residues in EC1+2 and equivalent positions throughout the extracellular repeats of protocadherin-15. Position of residue R113 is highlighted in red. Repeats EC6+7 and EC7+8 are most similar to EC1+2 and could be involved in interactions with cdh-23.



Supplementary Figure 19. Extracellular repeats of human cadherin-23 and binding interface. All 26 extracellular pairs of repeats are aligned to each other (EC1+2 to EC26+27). Boxes indicate interfacing residues in EC1+2 and equivalent positions throughout the extracellular repeats of cadherin-23. Position of residue E77 is highlighted in red. Repeats EC6+7 are the most similar to repeats EC1+2 and could be involved in interactions with pcdh-15.

Supplementary References

50. Harrison, O. J. et al. Two-step adhesive binding by classical cadherins. *Nat. Struct. Mol. Biol.* **17**, 348–357 (2010).
51. Katsamba, P. et al. Linking molecular affinity and cellular specificity in cadherin-mediated adhesion. *Proc. Natl. Acad. Sci. USA*, **106**, 11594–11599 (2009).
52. Brasch, J. et al. Structure and binding mechanism of vascular endothelial cadherin: a divergent classical cadherin. *J. Mol. Biol.*, **408**, 57–73 (2011).
53. Sotomayor, M., Corey, D. P. and Schulten, K. In search of the hair-cell gating spring: elastic properties of ankyrin and cadherin repeats. *Structure*, **13**, 669–682 (2005).
54. Lee, G. et al. Nanospring behaviour of ankyrin repeats. *Nature*, **440**, 246–249 (2006).
55. Li, L., Wetzel, S., Plückthun, A. and Fernandez, J. M. Stepwise unfolding of ankyrin repeats in a single protein revealed by atomic force microscopy. *Biophys. J.*, **90**, L30–L32 (2006).
56. Oroz, J. et al. Nanomechanics of the cadherin ectodomain: “canalization” by Ca^{2+} binding results in a new mechanical element. *J. Biol. Chem.* **286**, 9405–9418 (2011).
57. Corey, D. P. and Hudspeth, A. J. Kinetics of the receptor current in bullfrog saccular hair cells. *J. Neurosci.* **3**, 962–976 (1983).
58. Karplus, M. and Petsko, G.A. Molecular dynamics simulations in biology. *Nature*, **347**, 631–639.
59. Schwander, M. et al. A mouse model for nonsyndromic deafness (DFNB12) links hearing loss to defects in tip links of mechanosensory hair cells. *Proc. Natl. Acad. Sci. USA* **106**, 5252–5257 (2009).
60. Vendome, J., et al. Molecular design principles underlying β -strand swapping in the adhesive dimerization of cadherins. *Nat. Struct. Mol. Biol.* **18**, 693–700 (2011).
61. Pokutta S, Herrenknecht, K., Kemler, R., and Engel, J. Conformational changes of the recombinant extracellular domain of E-cadherin upon calcium binding. *Eur. J. Biochem.* **223**, 1019–1026 (1994).
62. Cailliez, F. and Lavery, R. Cadherin mechanics and complexation: the importance of calcium binding. *Biophys. J.* **89**, 3895–3903 (2005).
63. Vunnam, N., Flint, J., Balbo, A., Schuck, P., and Pedigo, S. Dimeric states of neural- and epithelial-cadherins are distinguished by the rate of disassembly. *Biochemistry* **50**, 2951–2961 (2011).
64. Kim, S. A., Tai, C. Y., Mok, L. P., Mosser, E. A., and Schuman, E. M. Calcium-dependent dynamics of cadherin interactions at cell-cell junctions. *Proc. Natl. Acad. Sci. USA* **108**, 9857–9862 (2011).
65. Vunnam, N. and Pedigo, S. Sequential binding of calcium leads to dimerization in neural cadherin. *Biochemistry* **50**, 2973–2982 (2011).
66. Huertas-Vazquez, A. et al. A nonsynonymous SNP within PCDH15 is associated with lipid traits in familial combined hyperlipidemia. *Hum. Genet.* **127**, 83–89 (2009).
67. Grossman, S. R. et al. A composite of multiple signals distinguishes causal variants in regions of positive selection. *Science*. **327**, 883–886 (2010).
68. Ciatto, C., et al. T-cadherin structures reveal a novel adhesive binding mechanism. *Nat. Struct. Mol.*

Biol. **17**, 339-347 (2010).

69. Boggon, T. J., et al. C-cadherin ectodomain structure and implications for cell adhesion mechanisms. *Science*, **296**, 1308-1313 (2002).

70. Patel, S.D., et al. Type II cadherin ectodomain structures: implications for classical cadherin specificity. *Cell*, **124**, 1255-1268 (2006).

71. Ahmed, Z. M. et al. PCDH15 is expressed in the neurosensory epithelium of the eye and ear and mutant alleles are responsible for both USH1F and DFNB23. *Hum. Mol. Genet.* **12**, 3215-3223 (2003).

72. Doucette, L. et al. Profound, prelingual nonsyndromic deafness maps to chromosome 10q21 and is caused by a novel missense mutation in the Usher syndrome type IF gene PCDH15. *Eur. J. Hum. Genet.* **17**, 554-564 (2009).